

Global endwall effects on centrifugally stable flows

Marc Avila,¹ Matt Grimes,² Juan M. Lopez,² and Francisco Marques¹

¹*Departament de Física Aplicada, Universitat Politècnica de Catalunya, 08034 Barcelona, Spain*

²*Department of Mathematics and Statistics, Arizona State University, Tempe, Arizona 85287, USA*

(Received 13 May 2008; accepted 4 September 2008; published online 13 October 2008)

We investigate the stability of a fluid confined between two cylinders that rotate at same constant angular speed. In the case of infinite cylinders, or endwalls rotating with the cylinders, the flow is in solid-body rotation and hence linearly stable for any rotation speed. However, when the endwalls are stationary, a large-scale circulation is driven by radially inward boundary layer flow on the endwalls. For sufficiently high angular speeds, this circulation becomes unstable to azimuthal waves. As the length-to-gap aspect ratio of the system is increased, a wealth of instabilities is revealed. It is particularly interesting that for all these instabilities the associated energy is localized in the equatorial region, as far from the endwalls as possible. This shows that care must be taken when assuming localized endwall effects in simplified models. © 2008 American Institute of Physics. [DOI: 10.1063/1.2996326]

I. INTRODUCTION

Flow in the annular gap between two rotating cylinders has been a paradigm problem in fluid dynamics and central to many developments in the field. The theoretical and numerical analysis of this system, known as the Taylor–Couette flow, is greatly simplified when the length-to-gap aspect ratio Γ is assumed to be infinite, endowing the system with translation invariance in the axial direction. Under this assumption, the Navier–Stokes equations admit a basic flow which consists of a pure azimuthal shear, circular Couette flow. For stationary outer cylinder and rotating inner cylinder, the radial distribution of angular momentum of the Couette flow is centrifugally unstable, and when the Reynolds number Re is large enough, the system forms radial jets that transport angular momentum from the inner cylinder boundary layer to the outer cylinder. The resulting secondary steady flow consists of an infinite array of pairs of counter-rotating cells, which is periodic in the axial direction. This cellular pattern is known as the Taylor-vortex flow.

In a laboratory experiment the presence of endwalls destroys the axial translational symmetry. Moreover, the equations of fluid motion are elliptic so effects from the boundaries are felt over the entire annular domain.¹ Therefore, it is not surprising that an important part of literature on the subject has been devoted to determining finite-length effects. The predicted onset of centrifugal instability for infinite cylinders is in good agreement with experimental apparatuses of aspect ratios as low as $\Gamma=8$. Nevertheless, one needs $\Gamma=40$ to obtain quantitative agreement for the threshold of the secondary instability.² For endwalls at rest, the no-slip boundary conditions of a physical apparatus generate a boundary layer flow driven by the discontinuity in azimuthal velocity at the junctions between the rotating inner cylinder and stationary endwalls. This boundary layer flow is radially inward and generates a toroidal vortex adjacent to each endwall. On increasing Re , the vortices become stronger and excite centrifugal instability, resulting in a cellular flow which eventually fills the apparatus, the normal Taylor-vortex flow.

Anomalous cellular patterns with a radially outward boundary layer flow may also be obtained.^{1,3–6} The competition between anomalous and normal cellular flows has been extensively studied for $\Gamma \sim 1$,^{4,7–10} and a comprehensive understanding of the dynamics has emerged.¹¹ The interaction between endwall effects and centrifugal instability has been investigated considering several different boundary conditions at the endwalls.¹² More recently, new classes of spiral flows that only exist when endwalls are present have been found in counter-rotating regimes.^{13,14} These spiral flows compete with the classic spirals from linear stability analysis,¹⁵ which are confined by endwall vortices.¹⁶

Common to these studies is the investigation of regimes dominated by the centrifugal instability. When the two cylinders rotate at the same angular speed, in the limit of infinite aspect ratio, the flow is in solid-body rotation and is stable to infinitesimal perturbations. In the finite case, the solid-body rotation state is lost as soon as there is any difference between the angular speed of endwalls and cylinders. When the endwalls are rotating at a different rate from the ambient rotation, Ekman layers form on the endwalls, and in the limit of stationary endwalls, Bödewadt boundary layers form.¹⁷ All of the analyses of these boundary layers (which impose solid-body rotation far from the layers) suggest that the effects are local to the boundary layers,^{18,19} and confined Bödewadt flows in cylinders also suggest localized effects.^{20–22}

Bödewadt boundary layers in centrifugally stable annular configurations allow one to investigate the global effect of these types of boundary layers in enclosed flows. In particular, the question we wish to address here is as follows: How does the presence of stationary endwalls manifest itself in the otherwise stable solid-body rotation configuration? We have found that the presence of stationary endwalls with cylinders both rotating at the same angular rate (the Bödewadt setting) drives a large-scale circulation which fills the entire annular region, and furthermore, that the primary instability is not localized near the endwalls but rather manifests itself

as far as possible from them at the equator, precisely where it has usually been hoped that the presence of endwalls would be minimal.

II. GOVERNING EQUATIONS AND NUMERICAL METHODS

Consider an incompressible fluid of kinematic viscosity ν confined between two concentric cylinders of length h and inner and outer radii r_i^* and r_o^* . The two cylinders rotate at the same constant angular speed Ω , whereas the top and bottom endwalls remain at rest. The system is nondimensionalized using the gap, $d=r_o^*-r_i^*$, as the length scale and Ω^{-1} as the time scale. The dynamics are governed by three parameters,

$$\text{Reynolds number: } \text{Re} = \Omega d r_o^* / \nu,$$

$$\text{aspect ratio: } \Gamma = h/d,$$

$$\text{radius ratio: } \delta = r_i^*/r_o^*.$$

In this study, we fix the radius ratio at $\delta=0.5$, yielding non-dimensional inner and outer radii of $r_i=1$ and $r_o=2$, respectively.

The flow is governed by the incompressible Navier–Stokes equations

$$\partial_t \mathbf{v} + (\mathbf{v} \cdot \nabla) \mathbf{v} = -\nabla p + \frac{1}{\text{Re}} \Delta \mathbf{v}, \quad \nabla \cdot \mathbf{v} = 0. \quad (1)$$

In cylindrical coordinates, (r, θ, z) , the nondimensional velocity is $\mathbf{v}=(u, v, w)$ and the corresponding vorticity is $\nabla \times \mathbf{v}=(\xi, \eta, \zeta)$. The no-slip boundary conditions are

$$\mathbf{v}(r_i, \theta, z, t) = (0, \delta, 0),$$

$$\mathbf{v}(r_o, \theta, z, t) = (0, 1, 0), \quad (2)$$

$$\mathbf{v}(r, \theta, \pm \Gamma/2, t) = (0, 0, 0).$$

The governing equations and boundary conditions are invariant under arbitrary rotations R_ϕ about the axis, and the reflection K_z about the equatorial plane $z=0$. The actions of these symmetries on the velocity field are

$$R_\phi \mathbf{v}(r, \theta, z, t) = \mathbf{v}(r, \theta + \phi, z, t), \quad (3)$$

$$K_z \mathbf{v}(r, \theta, z, t) = (u, v, -w)(r, \theta, -z, t). \quad (4)$$

Together, they generate the symmetry group $\mathcal{G}=SO(2) \times Z_2$ of the system.

A. Numerical formulation

The governing equation (1) has been solved using a second order time-splitting method.²³ The spatial discretization is via a Galerkin–Fourier expansion in θ and Chebyshev collocation in $x=2r-r_i-r_o$ and $y=2z/\Gamma$, of the form

$$F(r, \theta, z) = \sum_{l=0}^L \sum_{n=0}^N \sum_{m=0}^M a_{l,n,m} T_l(x) T_n(y) e^{im\theta}, \quad (5)$$

where the function $f=\text{real}(F)$ represents the three velocity components and pressure. For each Fourier mode in Eq. (5),

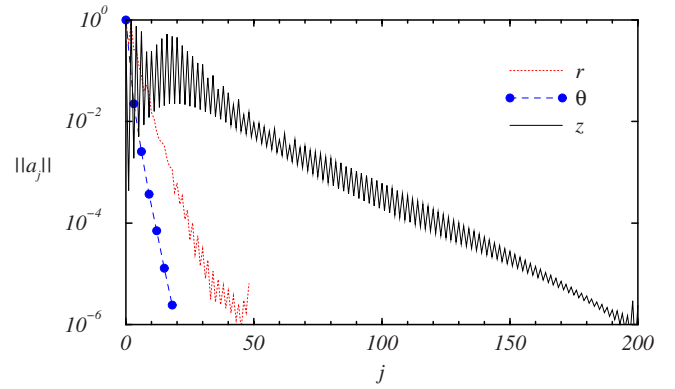


FIG. 1. (Color online) Convergence of the spectral coefficients in Eq. (5) of the radial velocity using the infinity norm. The flow corresponds to a rotating wave with azimuthal wavenumber $m=3$ at $\text{Re}=1800$ and $\Gamma=6$, computed with $L=48$ Chebyshev radial points, $M=18$ Fourier modes, and $N=200$ Chebyshev axial points.

the corresponding Helmholtz and Poisson equations are solved efficiently by using a complete diagonalization of the operators in both the radial and axial directions. Note that to decouple the Helmholtz equations for u and v , we have used the combinations $u_+ = u + iv$ and $u_- = u - iv$.²⁴

The idealized boundary conditions in Eq. (2) are discontinuous at the junctions where the stationary endwalls meet the rotating cylinders, $(r=r_i, z=\pm \Gamma/2)$ and $(r=r_o, z=\pm \Gamma/2)$. In a physical experiment there are small but finite gaps at these junctions where the azimuthal velocity adjusts rapidly to zero. For an accurate use of spectral techniques, a regularization of these discontinuities is implemented of the form

$$v(r, \theta, \pm \Gamma/2, t) = \delta \exp\left(\frac{r_i - r}{\epsilon}\right) + \exp\left(\frac{r - r_o}{\epsilon}\right), \quad (6)$$

where ϵ is a small parameter that mimics the small physical gaps (we have used $\epsilon=0.006$). The use of $\epsilon \neq 0$ regularizes the otherwise discontinuous boundary conditions; see Ref. 25 for further details on the use of this technique in spectral codes.

The spectral solver used here is based on a previous scheme recently tested and used in a wide variety of flows in enclosed cylinders.^{26–28} We have checked the spectral convergence of the code using the infinity norm of the spectral coefficients of the computed solutions, defined as $\|a_l\|_\infty = \max_{n,m} |a_{l,n,m}|$ for the radial direction, and analogously for the axial and azimuthal directions. Figure 1 shows $\|a_j\|_\infty$, with $j=l, n, m$, of the radial velocity u for a $m=3$ rotating wave at $\text{Re}=1800$ and $\Gamma=6$. This solution has been computed with $L=48$ and $N=200$ Chebyshev points in r and z , and $M=18$ Fourier modes in θ . Overall, we have used up to $L=64$, $N=400$, and $M=75$ depending on Γ , Re , and the azimuthal wavenumber of the computed solutions, ensuring that the trailing coefficients of the spectral expansion (5) are at least five orders of magnitude smaller than the leading coefficients. Time steps as small as $\delta t=0.013$ have been required for numerical stability and accuracy of the second-order temporal scheme.

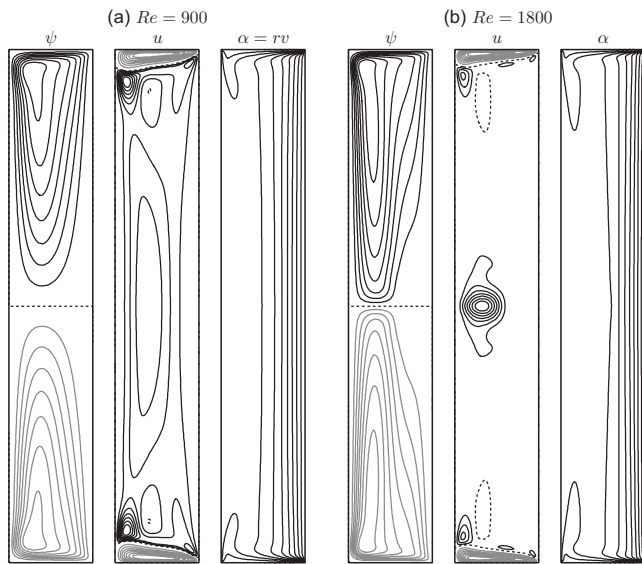


FIG. 2. Contours of ψ , u , and α in a meridional plane, $(r, z) \in [1, 2] \times [-3, 3]$, for the basic state at $\Gamma=6$ and (a) $Re=900$ and (b) 1800. Black (gray) corresponds to positive (negative) values, whereas the dotted lines correspond to the zero level.

III. BASIC STATE

For low Reynolds numbers the flow is steady, axisymmetric, and reflection symmetric about the equator, i.e., with symmetry group \mathcal{G} inherited from the system. Figure 2 shows contours, in a meridional plane, of the stream function ψ , radial velocity u , and angular momentum $\alpha=rv$ of the basic state for $\Gamma=6$ and $Re=900$ and 1800. The flow is characterized by two elongated counter-rotating circulation cells, illustrated by the streamlines ψ . This large-scale circulation is driven by a radial inflow, corresponding to negative radial velocity u in the stationary endwall boundary layers. Due to the presence of the inner cylinder, the fluid is forced to turn and flow along the inner cylinder, resulting in axial velocities driving fluid to the equatorial region. The fluid is recirculated to the outer cylinder and subsequently to its junctions with the endwalls, closing the streamlines.

In the case of endwalls rotating at the same angular speed as the cylinders, the fluid motion is purely azimuthal with angular momentum contours, $\alpha(r)=r^2/r_o$, corresponding to vortex lines that are parallel to the axis of rotation. However, in the case of stationary endwalls, the fluid is no longer in solid-body rotation but in a Bödewadt boundary layer configuration. The vortex lines are tangential to the stationary endwalls and they emanate and terminate at the corners (see contours of α in Fig. 2). Near the endwalls, the vortex lines bend in the radial direction and generate strong axial gradients of α which ultimately produce a radial inflow in the endwall boundary layers,^{17,21} shown as gray contours of radial velocity in Fig. 2. Figure 3 shows profiles of azimuthal and radial velocity at midgap $r=1.5$ close to the wall at $z=-\Gamma/2$; the axial coordinate z has been scaled with $Re^{0.5}$, illustrating the expected Bödewadt boundary layer velocity profiles and thickness scaling.

For low Reynolds numbers, endwall effects do not propagate far into the interior. Although the basic state con-

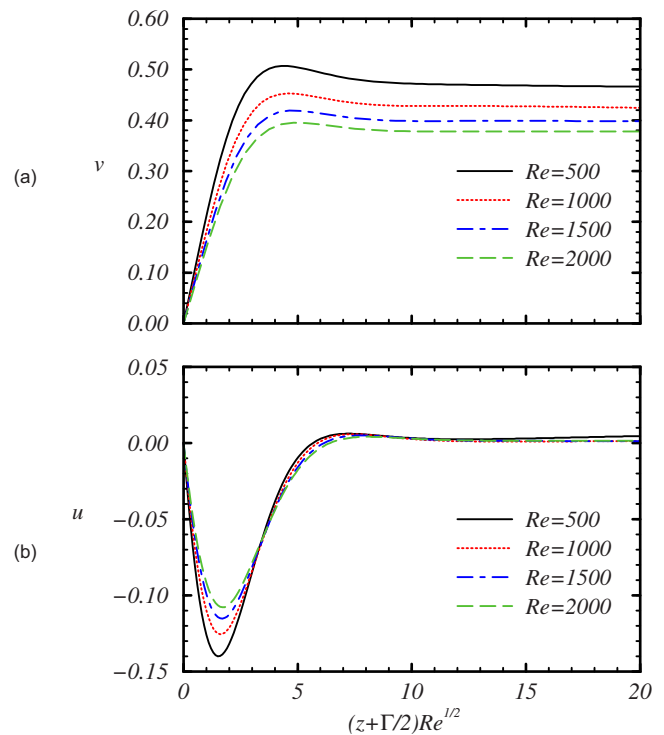


FIG. 3. (Color online) Axial profiles of v and u at midgap $r=1.5$ close to the wall at $z=-\Gamma/2$ for $\Gamma=6$ and Re as indicated.

sists of a large-scale circulation, the meridional flow is slow outside the boundary layers. Figure 4(a) shows profiles of the axial velocity w close to the inner cylinder, at $r=1.1$, for various Re . At $Re=500$, large axial velocities are confined near the endwalls and gradually decrease in magnitude toward the equator, where $w=0$. However, as Re is increased, the axial velocity tends to be constant outside the endwall boundary layers. This results in large axial velocities of opposite sign in the equatorial region which strengthen the radial flow at the equator. Figure 4(b) shows profiles of u at the equator for the same Reynolds numbers as in Fig. 4(a). The strength of the radial outflow remains essentially unchanged up to about $Re=1200$. However, for $Re > 1200$ endwall effects are no longer localized, generating a strong radial swirling jet which extends from the inner cylinder to about midgap. The variation of the maximum radial velocity at the equator, $U_{\max}=\max[u(r, z=0)]$, for $Re \in [0, 2000]$ is plotted in Fig. 5, illustrating the change in behavior at about $Re=1200$. This change can also be observed in the contours of radial velocity in Fig. 2, where for low Re the radial flow in the interior is seen to consist of a weak effusive flow out of the inner cylinder, whereas for higher Re an equatorial swirling jet forms and strengthens linearly with Re .

IV. INSTABILITY OF THE EQUATORIAL JET

For sufficiently high Reynolds numbers the steady basic state becomes unstable and more complex secondary flows appear. According to the equivariant branching lemma,²⁹ the symmetry group of the basic state determines the type of symmetry breaking bifurcations that may occur. For the

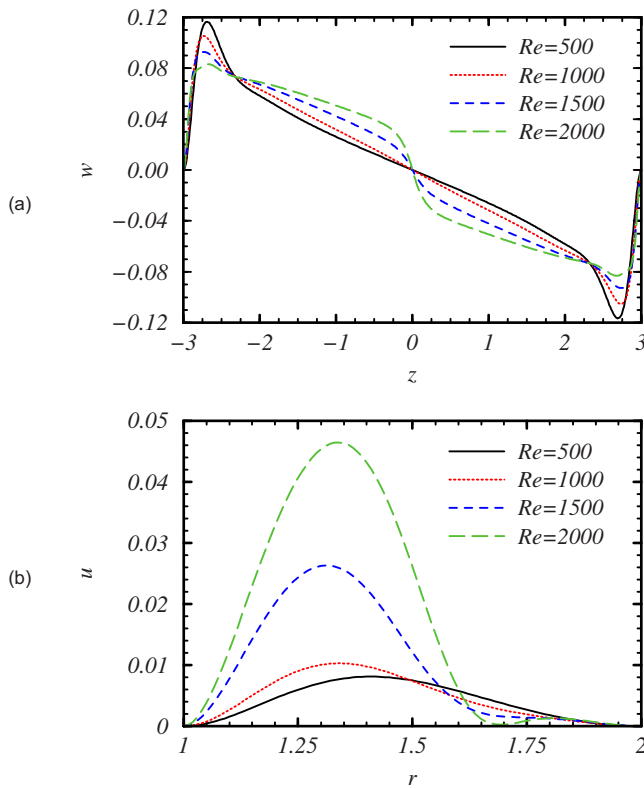


FIG. 4. (Color online) Profiles of (a) w at $r=1.1$ and (b) u at $z=0$ for the basic state at $\Gamma=6$ and Re as indicated.

range of aspect ratios $\Gamma \in [2, 10]$ investigated here, the steady basic state becomes unstable via a supercritical Hopf bifurcation to nonaxisymmetric time-periodic flow when increasing the Reynolds number. The Hopf bifurcation breaks the continuous rotational symmetry R_ϕ , which becomes equivalent to a time translation

$$\mathbf{v}(r, \theta, z, t) = R_\phi \mathbf{v}(r, \theta, z, t - \phi m / \omega). \quad (7)$$

The bifurcating state is a rotating wave with Hopf frequency ω and azimuthal wavenumber m . Moreover, it is invariant under discrete rotations of angle $\phi = 2\pi/m$, $R_{2\pi/m}$, that generate the generic symmetry group Z_m of a rotating wave RW_m emerging from a $SO(2)$ -Hopf bifurcation.²⁹ The precise manner in which the additional reflection symmetry of the basic state is broken or preserved in the bifurcation dis-

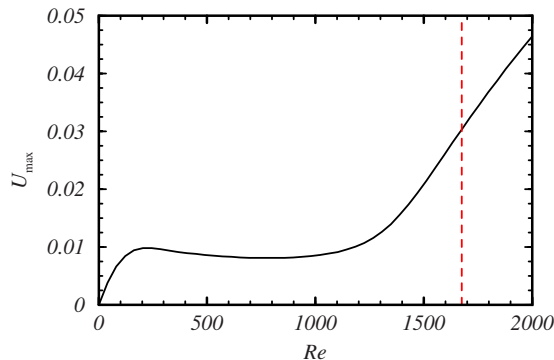


FIG. 5. (Color online) Variation of U_{\max} with Re for $\Gamma=6$. The dashed line corresponds to the onset of three-dimensional flow (RW_3) at $Re_c=1674$.

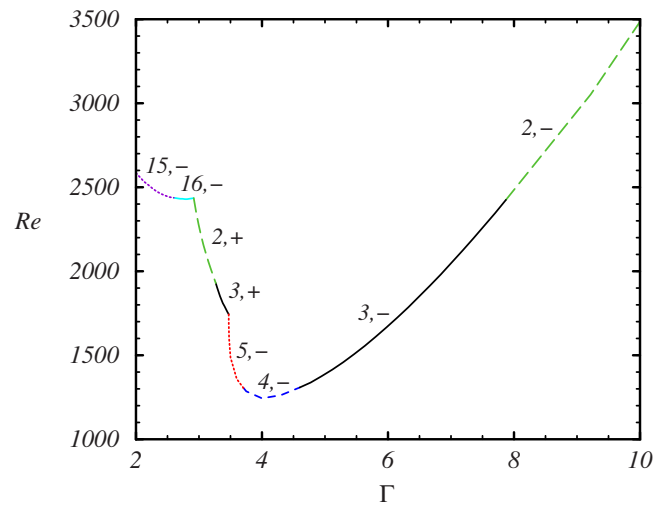


FIG. 6. (Color online) Critical Reynolds number, Re_c , as a function of the distance between the endwalls, Γ . The critical azimuthal wavenumber m of the bifurcating state is indicated above each curve. The type of rotating wave is denoted as $-$ ($+$) corresponding to broken (preserved) reflection Z_2 symmetry. Not shown in the figure, the critical azimuthal wavenumber changes from $m=15$ to $m=14$ at $\Gamma=2$.

tinguishes the different modes of instability. If K_z is preserved the rotating wave has the symmetry group $Z_m \times Z_2$ and will be termed RW_m^+ . When K_z is broken, the rotating wave RW_m^- is still invariant to a combination of the reflection symmetry K_z and a rotation of $R_{\pi/m}$, and the symmetry group is now Z_{2m} .³⁰

The bifurcation curves have been computed by linear stability methods, determining the growth rates of perturbations with the appropriate symmetries, i.e., working in the symmetric subspaces invariant to $Z_m \times Z_2$ or Z_{2m} . We have obtained a critical curve for each type of perturbation. Figure 6 shows the lower envelope of these curves, which is the stability curve of the basic state, $Re_c(\Gamma)$, for $\Gamma \in [2, 10]$. The different sections of $Re_c(\Gamma)$ are labeled with (m, \pm) indicating a bifurcation to RW_m^\pm . The points where two of the sections meet are bicritical points, double Hopf bifurcations where two different rotating waves bifurcate simultaneously. The double Hopf bifurcation has associated very rich nonlinear dynamics in its neighborhood. Depending on the particulars of the system under consideration, there are many different dynamical scenarios, including quasiperiodic and three-tori solutions, and heteroclinic connections resulting in chaotic dynamics.³¹ In the present problem, the presence of several double Hopf bifurcations strongly suggest that complex dynamics is likely to occur beyond the critical curve in Fig. 6.

A. Moderate to large aspect ratio instability

For moderate to large aspect ratios, $\Gamma > 3.475$, the bifurcating rotating waves break the reflection symmetry K_z . However, they are invariant under K_z composed with a rotation of angle $\phi = \pi/m$. The action of this symmetry on the velocity field is

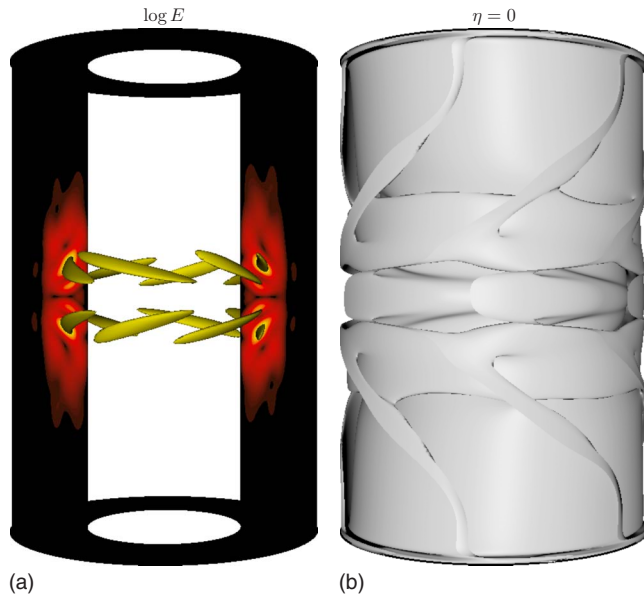


FIG. 7. (Color online) (a) Kinetic energy distribution E logarithmic color map of RW_3^- at $\Gamma=6$ and $Re=1800$ (white corresponds to $E_{\max}=533$ and black to an energy level with $E < 10^{-3}E_{\max}$, and the three-dimensional isosurface corresponds to $E=400$). (b) The corresponding azimuthal vorticity $\eta=0$ isosurface. The axisymmetric component of the velocity field has been subtracted in both figures to aid in visualizing the three-dimensional structure of the flow (enhanced online).

$$K_z R_{\pi/m} \mathbf{v}(r, \theta, z, t) = (u, v, -w)(r, \theta + \pi/m, -z, t). \quad (8)$$

This spatial symmetry generates the complete symmetry group of the rotating waves, Z_{2m} . Note that the action of K_z and R_ϕ commute, and that $R_{2\pi/m} = (K_z R_{\pi/m})^2$, so Z_{2m} includes as a subgroup the generic symmetry group of a rotating wave, Z_m .

Figure 7(a) shows a logarithmic color map of the kinetic energy distribution, $E(r, \theta, z) = r(u^2 + v^2 + w^2)$, of a rotating wave with $m=3$, RW_3^- , at $\Gamma=6$ and $Re=1800$ after subtracting the axisymmetric component of the flow. The instability manifests in the equatorial swirling jet, where the kinetic energy is concentrated, whereas the endwall boundary layers remain steady and axisymmetric. The shape of RW_3^- is illustrated in Fig. 7(b), showing the $\eta=0$ three-dimensional isosurface of azimuthal vorticity. Figure 8(a) is a snapshot of

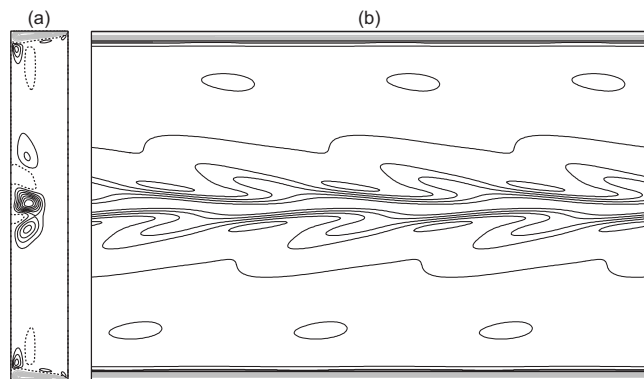


FIG. 8. Contours of radial velocity u in (a) a meridional plane $(r, z) \in [1, 2] \times [-3, 3]$ at $\theta=0$, and (b) a cylindrical surface $(\theta, z) \in [0, 2\pi] \times [-3, 3]$ at $r=1.5$. The flow is RW_3^- at $\Gamma=6$ and $Re=1800$.

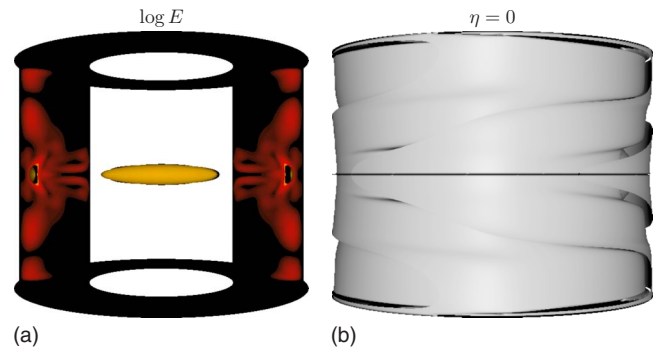


FIG. 9. (Color online) (a) Kinetic energy distribution E logarithmic color map of RW_2^+ at $\Gamma=3$ and $Re=2500$ (white corresponds to $E_{\max}=17\,198$ and black to an energy level with $E < 10^{-3}E_{\max}$, and the three-dimensional isosurface corresponds to $E=8600$). (b) Corresponding azimuthal vorticity $\eta=0$ isosurface. The axisymmetric component of the velocity field has been subtracted in both figures to aid in visualizing the three-dimensional structure of the flow (enhanced online).

the radial velocity u in the meridional plane $\theta=0$, which may be compared to Fig. 2(b) for the (unstable) basic state at same parameter values. The spatiotemporal behavior of RW_3^- consists of a periodic oscillation of the equatorial jet in the axial direction. The jets split in two, shedding spots of large positive radial velocity. This can be seen in Fig. 8(b) showing contours of u in a cylindrical surface (θ, z) at $r=1.5$. The action of the $K_z R_{\pi/m}$ symmetry (8) can be identified by advancing by an angle of $\pi/3$ and reflecting about the equator. Note that due to the spatiotemporal symmetry of rotating wave (7), Fig. 8(b) can also be interpreted as a space-time diagram, where a rotation of angle ϕ is equivalent to a time evolution of $t=3\phi/\omega$. The Hopf frequency is $\omega=1.514$, corresponding to a prograde precession speed of $\omega_p = \omega/m = 0.561$, i.e., approximately half the angular speed of the two cylinders.

In the case of $\Gamma=6$, the critical Reynolds number is $Re_c=1674$, with azimuthal wavenumber $m=3$. As the distance between endwalls is increased, the instability sets in at larger values of Re , as shown in Fig. 6. The wavenumber of the most dangerous RW_m^- decreases from $m=5$ at $\Gamma=3.475$ to $m=2$ at $\Gamma=10$, giving rise to double Hopf bifurcation points where the critical wavenumber changes.

B. Small aspect ratio instabilities

The Hopf bifurcation curve of Fig. 6 reaches a minimum at about $\Gamma=4$. Further decreasing the distance between endwalls results in a dramatic increase in Re_c down to $\Gamma=3.475$. At this point, the wavenumber of the most critical rotating wave changes from $m=5$ to $m=3$, corresponding to a different mode of instability. The Hopf bifurcations for $\Gamma < 3.475$ do not break the reflection symmetry and therefore are equivalent to generic $SO(2)$ -Hopf bifurcations. As a result, the emerging rotating waves are endowed with symmetry group $Z_m \times Z_2$ (whereas for $\Gamma > 3.475$, RW_m^- have Z_{2m} symmetry).

Figure 9(a) is a logarithmic color map of the kinetic energy distribution E of a rotating wave with $m=2$, RW_2^+ at

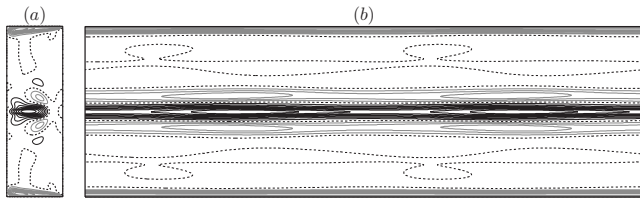


FIG. 10. Contours of radial velocity u in (a) a meridional plane $(r, z) \in [1, 2] \times [-1.5, 1.5]$ at $\theta=0$, and (b) a cylindrical surface $(\theta, z) \in [0, 2\pi] \times [-1.5, 1.5]$ at $r=1.5$. The flow is RW_2^+ at $\Gamma=3$ and $Re=2500$.

$\Gamma=3$ and $Re=2500$ after subtracting the axisymmetric component of the flow. The superscript, +, corresponds to preserved K_z symmetry. The corresponding isosurface of azimuthal vorticity $\eta=0$ is shown in Fig. 9(b). Note that as RW_m^+ is invariant under K_z , both azimuthal vorticity and axial velocity vanish at the equator, $\eta|_{z=0}=w|_{z=0}=0$. Therefore, there is no exchange of fluid between the upper and lower halves of the annulus. Figure 10(a) is a contour plot of u at the $\theta=0$ meridional cross section for the same RW_2^+ as in Fig. 9. The equatorial swirling jet seems to feel the presence of the endwalls, which prevent oscillations in the axial direction. Instead, the jet oscillates in the radial direction, causing the location of the maximum radial velocity, U_{\max} , to move back and forth along the equator. This motion is readily identified in Fig. 10(b), showing contours of u in a cylindrical surface. The amplitude of u at the equator fluctuates with θ . The precession speed of the wave, $\omega_p=0.0713$, is prograde but an order of magnitude slower than the angular velocity of the cylinders.

The wavenumber of the most unstable perturbation of the basic state jumps from $m=2$ to $m=16$ at $\Gamma=2.92$. This abrupt change corresponds to the appearance of a different mode of instability which breaks the K_z reflection symmetry. The emerging rotating waves have the same symmetry group, Z_{2m} , as the moderate aspect ratio cases. Figure 11(a) is a logarithmic color map of the kinetic energy distribution E of a rotating wave with $m=15$, RW_{15}^- , at $\Gamma=2.6$ and $Re=2600$ after subtracting the axisymmetric component of the flow. The corresponding isosurface of azimuthal vorticity $\eta=0$ is shown in Fig. 11(b). The breaking of the K_z symmetry

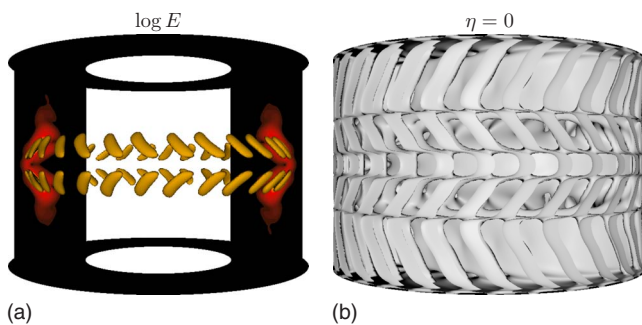


FIG. 11. (Color online) (a) Kinetic energy distribution E logarithmic color map of RW_{15}^- at $\Gamma=2.6$ and $Re=2600$ (white corresponds to $E_{\max}=3090$ and black to an energy level with $E < 10^{-3}E_{\max}$, and the three-dimensional isosurface corresponds to $E=1585$). (b) Corresponding azimuthal vorticity $\eta=0$ isosurface. The axisymmetric component of the velocity field has been subtracted in both figures to aid in visualizing the three-dimensional structure of the flow (enhanced online).

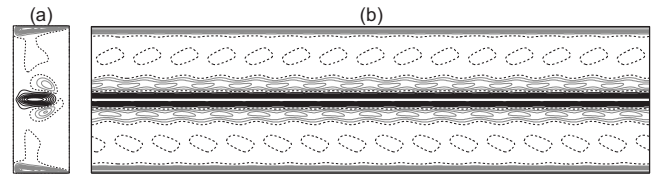


FIG. 12. Contours of radial velocity u in (a) a meridional plane $(r, z) \in [1, 2] \times [-1.3, 1.3]$ at $\theta=0$, and (b) a cylindrical surface $(\theta, z) \in [0, 2\pi] \times [-1.3, 1.3]$ at $r=1.5$. The flow is RW_{15}^- at $\Gamma=2.6$ and $Re=2600$.

is clear in Fig. 12(a), showing contours of u at the $\theta=0$ meridional plane. The positive radial velocity of the equatorial swirling jet is bounded by two asymmetric spots of negative radial velocity, shown in gray. In a cylindrical surface, these spots are seen to oscillate up and down with angle, whereas the jet itself remains axisymmetric and reflection symmetric. This is clearly seen in Fig. 12(b), showing contours of u at the $r=1.5$ cylindrical surface. The precession speed of the wave is $\omega_p=0.345$ (prograde).

V. CONCLUSIONS

The effects of Bödewadt type boundary layers in centrifugally stable annular flows have been investigated. The stationary endwalls, enclosed by the rotating cylinders, generate a radial inflow which induces a large-scale meridional circulation. In the low- Re regime, rapid fluid motion is confined to the endwall boundary layers. However, on increasing Re an equatorial swirling jet forms. The physical mechanism setting up this jet is now well understood: The Bödewadt flow in the endwall layers drives a large-scale circulation that advects angular momentum from the endwall layers at large radii in toward small radii and then along the inner cylinder boundary layer. This layer separates at midheight to form the equatorial swirling jet. For sufficiently large Re , the equatorial jet becomes unstable to azimuthal waves with prograde precession. Three distinct modes of instability, giving rise to rotating waves characterized by their wavenumber, precession speed, and spatial symmetries, have been revealed by varying the distance between endwalls, $\Gamma \in [2, 10]$. These new instabilities manifest, although in different manners, in the equatorial region, highlighting the global role of endwall boundary layers in confined annular flows.

Recent work in counter-rotating regimes has revealed two new spiral flows ($SPI_{+/-}$), whose amplitudes are localized near the endwalls.¹³ The $SPI_{+/-}$ can be distinguished by their spatial symmetries, identical to those of the rotating waves discussed in this paper. Moreover, these new states appear via Hopf bifurcations which are not predicted by linear stability analysis of circular Couette flow, i.e., under the infinite-cylinder approximation. For sufficiently large $\Gamma > 8$, the $SPI_{+/-}$ bifurcate at a Reynolds number independent of Γ and always before the classical spirals¹⁵ of the counter-rotating Taylor–Couette flow. After onset, the $SPI_{+/-}$ coexist with the classical spirals, which are present in the bulk of the apparatus. In a similar fashion, it would be interesting to investigate the competition between the Taylor-vortex flow and the rotating waves that we have found in the Bödewadt configuration.

It is well known that in swirling flows between cylinders, redistribution of the angular momentum introduced by the rotating walls results in a large variety of patterns.³² In the present problem, the presence of endwalls gives rise to the formation of an axisymmetric equatorial jet whose instabilities come in different flavors depending on the distance between endwalls. These instabilities are manifested via bifurcations which strongly depend on the symmetries of the system, while being independent of the physical mechanism (in the sense that these bifurcations are common to a vast array of flows and come about by different physical flow instabilities). The competition between these modes of instability is organized by codimension-two Hopf points, which lead to multiplicity of solutions and strong nonlinear interactions. Trying to assign a specific physical mechanism to each of the instabilities is a difficult task, beyond the scope of this work. This would require the analysis of the dynamics, a careful examination of the solutions obtained and investigation of the interactions between the bifurcated modes that will be addressed in the future.

ACKNOWLEDGMENTS

We wish to thank Dr. Jan Abshagen (University of Kiel) for sharing his experimental observations of rotating waves in moderate aspect ratio annuli, which inspired our numerical investigations. This work was supported by the National Science Foundation under Grant No. DMS-0505489, the Spanish Ministry of Education and Science under Grant Nos. FIS2007-61585, HA2005-0087, and AP-2004-2235, and the Catalanian Government under Grant No. SGR-00024. Part of the work was done during M. Avila's visit to the Department of Mathematics and Statistics, Arizona State University, whose kind hospitality is warmly appreciated. Computational resources of ASU's Fulton HPCI are greatly appreciated.

- ¹T. B. Benjamin, "Bifurcation phenomena in steady flows of a viscous fluid. I. Theory," *Proc. R. Soc. London, Ser. A* **359**, 1 (1978).
- ²J. A. Cole, "Taylor-vortex instability and annulus-length effects," *J. Fluid Mech.* **75**, 1 (1976).
- ³T. B. Benjamin, "Bifurcation phenomena in steady flows of a viscous fluid. II. Experiments," *Proc. R. Soc. London, Ser. A* **359**, 27 (1978).
- ⁴T. B. Benjamin and T. Mullin, "Anomalous modes in the Taylor experiment," *Proc. R. Soc. London, Ser. A* **377**, 221 (1981).
- ⁵K. A. Cliffe and T. Mullin, "A numerical and experimental study of anomalous modes in the Taylor experiment," *J. Fluid Mech.* **153**, 243 (1985).
- ⁶K. A. Cliffe, J. J. Kobine, and T. Mullin, "The role of anomalous modes in Taylor–Couette flow," *Proc. R. Soc. London, Ser. A* **439**, 341 (1992).
- ⁷K. A. Cliffe, "Numerical calculations of two-cell and single-cell Taylor flows," *J. Fluid Mech.* **135**, 219 (1983).
- ⁸G. Pfister, H. Schmidt, K. A. Cliffe, and T. Mullin, "Bifurcation phenomena in Taylor–Couette flow in a very short annulus," *J. Fluid Mech.* **191**, 1 (1988).

- ⁹G. Pfister, A. Schulz, and B. Lensch, "Bifurcations and a route to chaos of an one-vortex-state in Taylor–Couette flow," *Eur. J. Mech. B/Fluids* **10**, 247 (1991).
- ¹⁰G. Pfister, Th. Buzug, and N. Enge, "Characterization of experimental time series from Taylor–Couette flow," *Physica D* **58**, 441 (1992).
- ¹¹T. Mullin, Y. Toya, and S. J. Tavener, "Symmetry-breaking and multiplicity of states in small aspect ratio Taylor–Couette flow," *Phys. Fluids* **14**, 2778 (2002).
- ¹²O. Czarny, E. Serre, P. Bontoux, and R. M. Lueptow, "Interaction between Ekman pumping and the centrifugal instability in Taylor–Couette flow," *Phys. Fluids* **15**, 467 (2003).
- ¹³M. Heise, J. Abshagen, D. Küter, K. Hochstrate, and G. Pfister, "Localized spirals in Taylor–Couette flow," *Phys. Rev. E* **77**, 026202 (2008).
- ¹⁴M. Heise, C. Hoffmann, J. Abshagen, A. Pinter, G. Pfister, and M. Lücke, "Stabilization of domain walls between traveling waves by nonlinear mode coupling in Taylor–Couette flow," *Phys. Rev. Lett.* **100**, 064501 (2008).
- ¹⁵W. F. Langford, R. Tagg, E. J. Kostelich, H. L. Swinney, and M. Golubitsky, "Primary instabilities and bicriticality in flow between counter-rotating cylinders," *Phys. Fluids* **31**, 776 (1988).
- ¹⁶C. Hoffmann, M. Lücke, and A. Pinter, "Spiral vortices traveling between two rotating defects in the Taylor–Couette system," *Phys. Rev. E* **72**, 056311 (2005).
- ¹⁷U. T. Bödewadt, "Rotary currents on fixed grounds," *Z. Angew. Math. Mech.* **20**, 241 (1940).
- ¹⁸P. J. Zandbergen and D. Dijkstra, "Von Kármán swirling flows," *Annu. Rev. Fluid Mech.* **19**, 465 (1987).
- ¹⁹R. J. Lingwood, "Absolute instability of the Ekman layer and related rotating flows," *J. Fluid Mech.* **331**, 405 (1997).
- ²⁰Ö. Savaş, "Stability of Bödewadt flow," *J. Fluid Mech.* **183**, 77 (1987).
- ²¹J. M. Lopez and P. D. Weidman, "Stability of stationary endwall boundary layers during spindown," *J. Fluid Mech.* **326**, 373 (1996).
- ²²J. M. Lopez, "Flow between a stationary and a rotating disk shrouded by a co-rotating cylinder," *Phys. Fluids* **8**, 2605 (1996).
- ²³S. Hughes and A. Randriamampianina, "An improved projection scheme applied to pseudospectral methods for the incompressible Navier–Stokes equations," *Int. J. Numer. Methods Fluids* **28**, 501 (1998).
- ²⁴S. A. Orszag and A. T. Patera, "Secondary instability of wall-bounded shear flows," *J. Fluid Mech.* **128**, 347 (1983).
- ²⁵J. M. Lopez and J. Shen, "An efficient spectral-projection method for the Navier–Stokes equations in cylindrical geometries I. Axisymmetric cases," *J. Comput. Phys.* **139**, 308 (1998).
- ²⁶F. Marques, I. Mercader, O. Batiste, and J. M. Lopez, "Centrifugal effects in rotating convection: Axisymmetric states and three-dimensional instabilities," *J. Fluid Mech.* **580**, 303 (2007).
- ²⁷J. M. Lopez, F. Marques, I. Mercader, and O. Batiste, "Onset of convection in a moderate aspect-ratio rotating cylinder: Eckhaus–Benjamin–Feir instability," *J. Fluid Mech.* **590**, 187 (2007).
- ²⁸I. Mercader, A. Alonso, and O. Batiste, "Spatio-temporal dynamics near the onset of convection for binary mixtures in cylindrical containers," *Phys. Rev. E* **77**, 036313 (2008).
- ²⁹M. Golubitsky, I. Stewart, and D. G. Schaeffer, *Singularities and Groups in Bifurcation Theory. Volume II*, Applied Mathematical Sciences Vol. 69 (Springer-Verlag, New York, 1988).
- ³⁰J. M. Lopez and F. Marques, "Mode competition between rotating waves in a swirling flow with reflection symmetry," *J. Fluid Mech.* **507**, 265 (2004).
- ³¹Y. A. Kuznetsov, *Elements of Applied Bifurcation Theory*, 3rd ed. (Springer, New York, 2004).
- ³²C. D. Andereck, S. S. Liu, and H. L. Swinney, "Flow regimes in a circular Couette system with independently rotating cylinders," *J. Fluid Mech.* **164**, 155 (1986).